

## ARTICLE OPEN



# Cyclic production of biocompatible few-layer graphene ink with in-line shear-mixing for inkjet-printed electrodes and Li-ion energy storage

Tian Carey<sup>1,2</sup>, Abdelnour Alhourani<sup>3</sup>, Ruiyuan Tian<sup>2</sup>, Shayan Seyedin<sup>4</sup>, Adrees Arbab<sup>1</sup>, Jack Maughan<sup>2</sup>, Lidija Šiller<sup>4</sup>, Dominik Horvath<sup>2</sup>, Adam Kelly<sup>2</sup>, Harneet Kaur<sup>2</sup>, Eoin Caffrey<sup>2</sup>, Jong M. Kim<sup>1</sup>, Hanne R. Hagland<sup>3</sup> and Jonathan N. Coleman<sup>2</sup>

The scalable production of two-dimensional (2D) materials is needed to accelerate their adoption to industry. In this work, we present a low-cost in-line and enclosed process of exfoliation based on high-shear mixing to create aqueous dispersions of few-layer graphene, on a large scale with a  $Y_w \sim 100\%$  yield by weight and throughput of  $\phi \sim 8.3 \text{ g h}^{-1}$ . The in-line process minimises basal plane defects compared to traditional beaker-based shear mixing which we attribute to a reduced Reynolds number,  $Re \sim 10^5$ . We demonstrate highly conductive graphene material with conductivities as high as  $\sigma \sim 1.5 \times 10^4 \text{ S m}^{-1}$  leading to sheet-resistances as low as  $R_s \sim 2.6 \Omega \square^{-1}$  ( $t \sim 25 \mu\text{m}$ ). The process is ideal for formulating non-toxic, biocompatible and highly concentrated ( $c \sim 100 \text{ mg ml}^{-1}$ ) inks. We utilise the graphene inks for inkjet printable conductive interconnects and lithium-ion battery anode composites that demonstrate a low-rate lithium storage capability of  $370 \text{ mAh g}^{-1}$ , close to the theoretical capacity of graphite. Finally, we demonstrate the biocompatibility of the graphene inks with human colon cells and human umbilical vein endothelial cells at high  $c \sim 1 \text{ mg ml}^{-1}$  facilitating a route for the use of the graphene inks in applications that require biocompatibility at high  $c$  such as electronic textiles.

npj 2D Materials and Applications (2022)6:3; <https://doi.org/10.1038/s41699-021-00279-0>

## INTRODUCTION

Graphene and other 2D materials are expected to find major commercial applications in the coming years<sup>1</sup>. By utilising the unique electrical, optical, mechanical, chemical and thermal properties of 2D materials, additional functionality or improved performance can be added to many applications. Graphene could be useful in over 40 major application areas such as composites, energy storage, thermal management, sensors and coatings<sup>2</sup>. For example, graphene can be used as a barrier material for anti-corrosion<sup>3</sup>, an additive for mechanical reinforcement in polymers<sup>4</sup>, or as a conductive material in sensors<sup>5</sup>. Many of these applications will require few-layer graphene flakes (<10 layers) in large multiple quantities if successfully commercialised<sup>2</sup>. For example, if graphene flakes are used at low loading (~1%) in the 300 million tonnes per year global plastic industry<sup>6</sup>, or used to replace graphite (~10<sup>6</sup> tonnes per year)<sup>7</sup> in Li-ion batteries for the electric vehicle market it would create a demand of >1 kilotonne, far exceeding the global graphene supply<sup>8</sup>. Few-layer graphene flakes could also be utilised as a cost-reduction replacement material for metal components in applications such as interconnects or electrodes, particularly where form factor is important such as electronic textiles<sup>9</sup>.

Currently, printable metal inks (e.g. silver and gold) are commonly used as interconnect or electrode materials and are made of precious metals costing ~£1000 per litre on average and can have oxidation issues<sup>10</sup>, toxicity<sup>11</sup> or nanoparticle migration<sup>12</sup>, degrading device performance. Graphene inks could be potentially produced for as little as ~£20 per litre once scaled due to carbon's elemental abundance while retaining several functional

advantages when applied, such as flexibility, biocompatibility, environmental stability or weight reduction. The Hummers method emerged as one of the first methods to produce graphene in the form of graphene oxide (GO) flakes<sup>13</sup>. However, the GO flakes differ from pristine graphene, containing a population of functional groups that disrupt the sp<sup>2</sup> structure of graphite<sup>14</sup>. Liquid phase exfoliation (LPE) is established as the primary method to produce dispersions of pristine graphene flakes at scale and low cost<sup>15</sup>. The most common techniques to undertake exfoliation in liquid are ultrasonication<sup>16</sup>, ball milling<sup>17</sup>, shear-mixing<sup>18</sup>, electrochemical exfoliation<sup>19</sup>, wet-jet milling<sup>20</sup> and microfluidization<sup>21</sup>. To evaluate each technique's effectiveness, figures-of-merit (FOM) are frequently used to characterise the resulting dispersions. The yield by weight ( $Y_w$ ) is the ratio between the weight of the final graphene material and the starting graphite flakes<sup>22</sup>, while the throughput ( $\phi$ ) is defined as the mass of graphene obtained per hour. In the literature,  $Y_w$  and  $\phi$  are commonly used as FOM to assess the production process. Electrochemical exfoliation involves intercalating a 2D material such as graphite with an ionic species that expands and exfoliates the bulk material into flakes<sup>19,23,24</sup>. The process has high  $Y_w \sim 10\text{--}75\%$  with  $\phi \sim 0.3 \text{ g h}^{-1}$  when post-processing (e.g. material washing) is considered<sup>19,23,24</sup>. Ultrasonication is the most widely studied technique and typically involves using a bath sonicator<sup>16</sup>, which has been used to exfoliate graphene in toxic solvents (e.g. *n*-methyl-2-pyrrolidone, NMP)<sup>16</sup> and non-toxic (e.g. water) solvents<sup>25</sup>. However, ink concentrations,  $c$  up to  $\sim 1 \text{ mg ml}^{-1}$  in <24 h<sup>22</sup> equating to  $\phi \sim 1 \text{ g h}^{-1}$  and  $Y_w \sim 3\text{--}5\%$  has limited ultrasonication to lab-scale studies. Ball milling involves mixing

<sup>1</sup>Cambridge Graphene Center, Department of Engineering, University of Cambridge, Cambridge, UK. <sup>2</sup>CRANN and AMBER Research Centres, Trinity College Dublin, Dublin 2, Ireland. <sup>3</sup>Department of Chemistry, Bioscience and Environmental Engineering, University of Stavanger, Stavanger, Norway. <sup>4</sup>School of Engineering, Newcastle University, Newcastle upon Tyne, UK. ✉email: [tian.carey@cantab.net](mailto:tian.carey@cantab.net); [colemaj@tcd.ie](mailto:colemaj@tcd.ie)

graphite powder, solvent and zirconia/metal balls together in a rotatory mill. The friction and shear forces with the balls enable the exfoliation of graphite<sup>17</sup>. The  $\phi$  of the process is  $\sim 0.2 \text{ g h}^{-1}$  with a  $Y_w \sim 12\%$ <sup>17</sup>. Microchannel-based techniques such as microfluidization and wet-jet milling have also been used in cyclic processes to exfoliate graphene nanoplatelets and 2D materials with  $Y_w \sim 100\%$ <sup>20,21</sup>. Microfluidization involves using high pressure ( $\sim 250 \text{ MPa}$ ) to push a liquid through an interaction chamber with several micron-sized ( $\sim 87 \mu\text{m}$ ) channels generating high shear ( $>10^6 \text{ s}^{-1}$ )<sup>21</sup>. The liquid is cycled back through the interaction chamber over several hours to reach  $\phi \sim 9.3 \text{ g h}^{-1}$ <sup>21</sup>. Wet-jet milling is a similar technique which uses a hydraulic mechanism and piston at high pressure ( $\sim 250 \text{ MPa}$ ) to push liquid through perforated ( $\sim 100 \mu\text{m}$ ) discs<sup>20</sup>. The process has reached  $\phi \sim 23 \text{ g h}^{-1}$ <sup>20</sup>. However, in practice, the interaction chamber in these microchannel-based techniques can frequently become blocked by graphite. Unless addressed, this would decrease  $\phi$  in a commercial environment. Moreover, microfluidization systems are currently expensive ( $>£40,000$ ) and can overheat easily (even with active cooling) risking system damage. Processes such as ultrasonication, high-shear mixing and electrochemical exfoliation provide cheaper alternatives for 2D material production however their low  $\phi \sim 0.2\text{--}5.3 \text{ g h}^{-1}$  has made high-volume production of 2D materials difficult. Furthermore, ultrasonication and high-shear mixing have had challenges to scale as the hydrodynamic processes can damage the graphene basal plane after 2 h of processing<sup>26</sup>. Therefore, there is a need for a graphene production process which is reliable, produces pristine flakes free of basal plane defects and at a high  $Y_w$  and  $\phi$ . High-shear mixing could provide a route forward as it currently has minimal maintenance requirements and high  $\phi$ . Shear-mixing involves using a rotor (rotating blades) and stator (stationary screen) to generate shear forces to exfoliate material<sup>18</sup>. The shear-mixing process is typically undertaken in an open beaker ( $<1 \text{ L}$ ) or industrial-sized ( $>300 \text{ L}$ ) container<sup>18</sup>, and has demonstrated  $\phi \sim 5.3 \text{ g h}^{-1}$  but with a low  $Y_w \sim 0.001\%$ . Therefore, the graphene production process is still in need of significant improvement to fulfil the potential industrial scale demand. Furthermore, the low electrical conductivities of the resultant films ( $\sigma \sim 400 \text{ S m}^{-1}$ ) need to be improved for practical applications<sup>18</sup>. The engineering of conductive ink with a  $c > 1 \text{ mg ml}^{-1}$ ,  $\sigma > 10^3 \text{ S m}^{-1}$ ,  $\phi > 5 \text{ g h}^{-1}$ , defect-free and in a non-toxic solvent is highly desirable. In this work, we adapt the shear mixing process to recycle unexfoliated material to maximise  $\phi$ ,  $c$  and  $Y_w$ . While minimising  $Re < 10^6$  in our system reduces basal plane defects and maximises  $\sigma$  which enables the creation of applications such as inkjet printed interconnects and Li-ion batteries.

## RESULTS

### In-line shear-mixing process

We used an in-line shear mixing system (Silverson) to produce graphene flake dispersions (Fig. 1). In-line shear mixing is an enclosed, cyclic process where the rotor head's high-speed generates suction and drives the dispersion upwards into the rotor head. Centrifugal force pushes the graphite towards the rotor head's periphery and between the rotor (i.e. rotating blades) and the stator (i.e. a metal screen). The graphite experiences hydrodynamic stress which exfoliates the layered material and pushes it out and away from the rotor and stator. The system is self-pumping, and fresh material continually is drawn into the rotor head, which results in a cyclic flow of material through the system. Using this method, unexfoliated graphite is recycled by undergoing repeated hydraulic shearing. An ice bath or chiller can be used on the rubber tubing to maintain the system temperature. Furthermore, unlike standard shear mixing, the liquid is entirely enclosed.

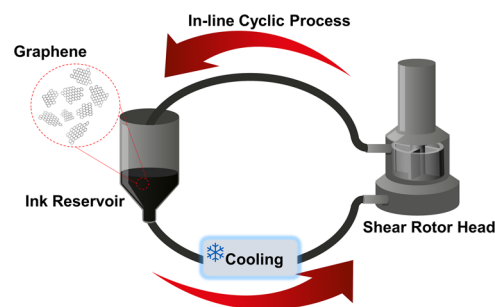


**Fig. 1 Schematic of the in-line shear mixing process.** Graphite, deionised water and SDC stabilisation agent are added to the reservoir. The shear rotor head pushes the material around the system while generating shear force, enabling the exfoliation of graphite into graphene.

We use graphite flakes as a starting material for the inks. We mix the flakes ( $100 \text{ mg ml}^{-1}$ ) with sodium deoxycholate (SDC,  $5 \text{ mg ml}^{-1}$ ) (Sigma-Aldrich) in deionised water ( $\sim 1 \text{ L}$ ) before adding to the in-line system. The temperature of the system increases over time once material passes through the rotor head. Therefore, an ice bath is used to keep the temperature at  $\sim 30^\circ \text{C}$ . Without cooling, the deionised water will evaporate, increase the liquid viscosity, decrease the liquid flow rate, and potentially damage the motor of the in-line shear-mixer. We define one cycle as the complete passthrough of the starting liquid volume ( $\sim 1000 \text{ ml}$ ) through the rotor head. Each cycle takes approximately  $10.8 \text{ s}$  to complete at  $8000 \text{ rpm}$  (i.e.  $1000 \text{ ml}$  passes through the system in  $10.8 \text{ s}$ , see Methods). We process the graphite and SDC dispersion for multiple cycle sets ( $2000$ ,  $4000$  and  $6000$  cycles). The process yields litre-scale dispersions of graphene ink with a high  $c$  of  $100 \text{ mg ml}^{-1}$  (measured on a microbalance, see Methods),  $Y_w \sim 100\%$  and  $\phi \sim 8.3 \text{ g h}^{-1}$ .

### Investigating flake lateral size, thickness and quality

After depositing the graphene ink on a silicon/silicon oxide ( $\text{Si/SiO}_2$ ) substrate, we use scanning electron microscopy (SEM) in Fig. 2 to determine the lateral size  $\langle L \rangle$  distribution of the graphite starting material (Fig. 2a) and its change in  $\langle L \rangle$  as a function of the number of processing cycles:  $2000$  (Fig. 2b),  $4000$  (Fig. 2c) and  $6000$  (Fig. 2d). We define the lateral size as  $\langle L \rangle = (xy)^{-1/2}$ , where  $x$  and  $y$  are the length and width of the flake<sup>27</sup>. For each processing cycle, we measure  $50$  flakes. The average lateral size is  $4.8 \pm 1.72 \mu\text{m}$ ,  $2.69 \pm 1.89 \mu\text{m}$ ,  $1.47 \pm 1.14 \mu\text{m}$  and  $0.65 \pm 0.48 \mu\text{m}$  for the dispersions of graphite,  $2000$ ,  $4000$  and  $6000$  cycles respectively, indicating a decreasing  $\langle L \rangle$  with processing (Fig. 2e). The size distribution characterised by standard deviation ( $\sigma_{sd}$ ) changes with processing cycles. The graphite's  $\sigma_{sd}$  before processing is  $1.72 \mu\text{m}$  which decreases to  $0.48 \mu\text{m}$  after  $6000$  cycles. It might be possible to narrow the lateral size distribution further by increasing the processing cycles. However, it might not be desirable as further processing will likely damage the basal plane of the graphene (see Raman spectroscopy section). We use atomic force microscopy (AFM) to further characterise the flakes and determine their apparent thickness and confirm  $\langle L \rangle$ . In Fig. 2f, AFM micrograph of a typical flake reveals thickness of  $8 \text{ nm}$  and  $\langle L \rangle \sim 270 \text{ nm}$ . We undertake AFM statistics in Fig. 2g and find the  $\langle L \rangle$  of  $30$  flakes after  $6000$  cycles. The flakes have a log-normal distribution<sup>28</sup> which peaks at  $386 \text{ nm}$  and has an average  $\langle L \rangle \sim 492 \text{ nm}$ , consistent with the SEM measurements. The flakes' apparent thickness is measured in Fig. 2h and shows a peak flake thickness of  $6.7 \text{ nm}$ , indicating that we have made few-layer graphene.

We use Raman spectroscopy to identify the flakes' quality as a function of the number of processing cycles. Figure 3a shows the

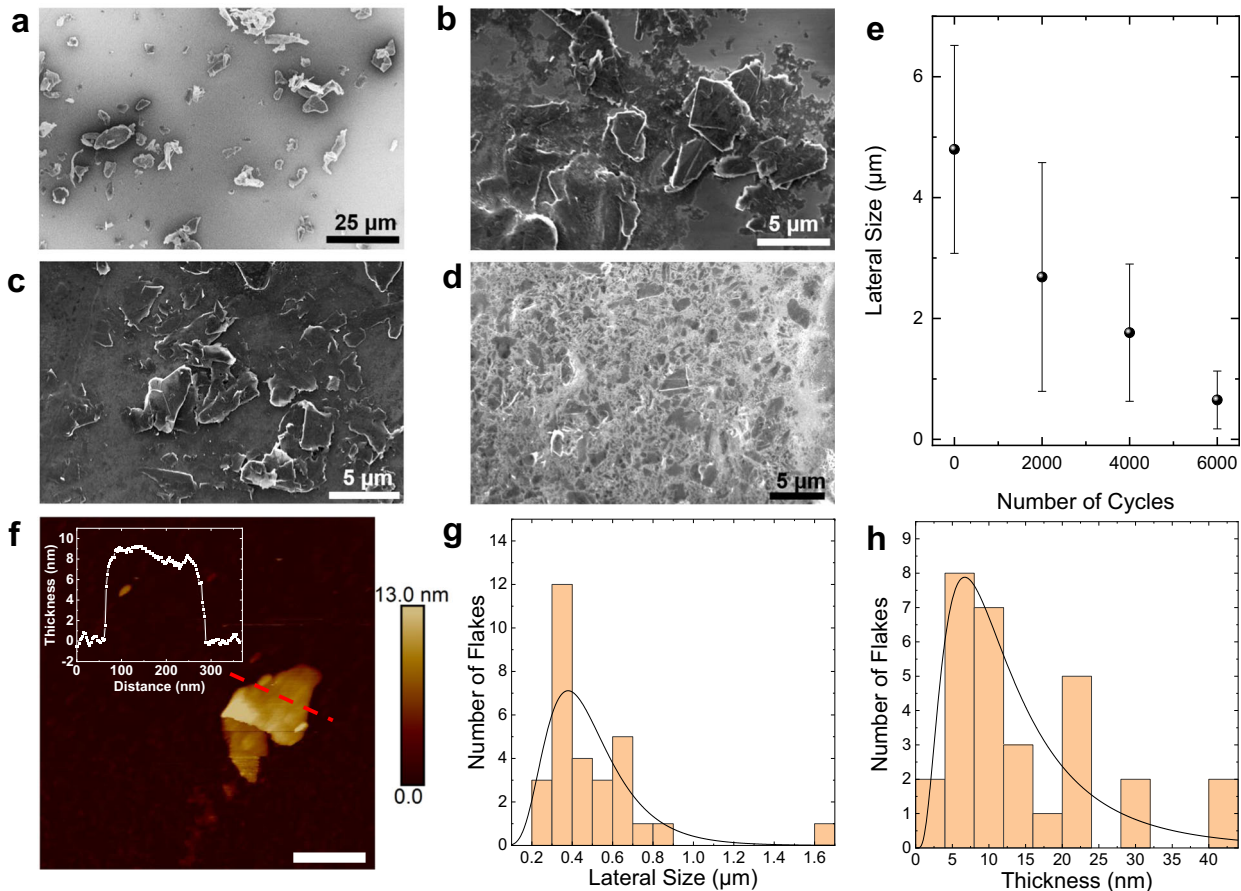


**Fig. 2 Examination of flake lateral size and thickness.** **a** SEM images of graphite. **b** 2000 cycles. **c** 4000 cycles. **d** 6000 cycles. **e** The lateral size distribution is plotted as a function of processing cycles, error is calculated as the standard deviation ( $n = 50$ ). **f** An AFM micrograph displaying a typical profile of a 6000 cycles graphene flake with a thickness of 8 nm and lateral size of 270 nm. The scale bar is 230 nm. **g** Lateral size and **h** thickness of the 6000 cycles graphene ink obtained from AFM analyses.

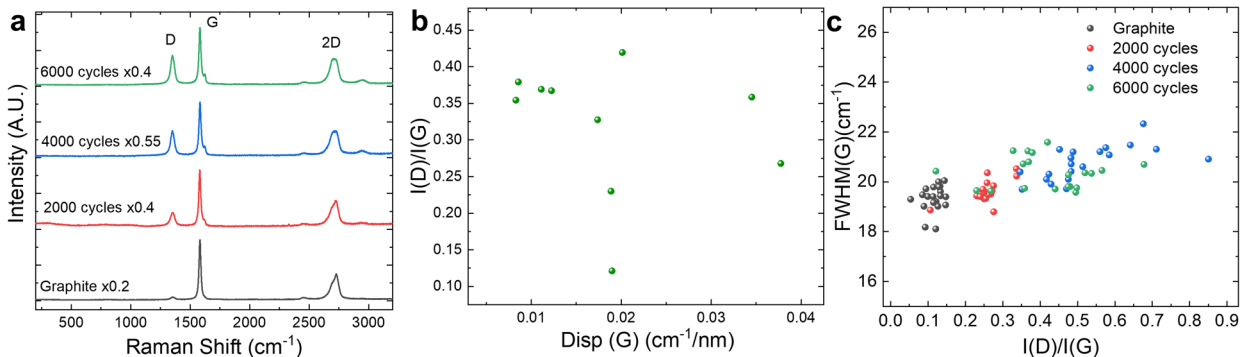


**Fig. 3 Examination of flake quality.** **a** Raman spectroscopy for graphite (black), 2000 (red), 4000 (blue) and 6000 (green) processing cycles. **b** The  $I(D)/I(G)$  ratio plotted as a function of the  $\text{Disp}(G)$  for 6000 processing cycles. **c**  $\text{FWHM}(G)$  plotted as a function of the  $I(D)/I(G)$  ratio.

spectra of the graphene with 2000 cycles (red curve), 4000 cycles (blue curve), 6000 cycles (green curve) and graphite (black curve). In the graphene spectra, the G peak located at  $\sim 1581 \text{ cm}^{-1}$ , corresponds to the  $E_{2g}$  phonon<sup>29</sup>. The D peak at  $\sim 1350 \text{ cm}^{-1}$  is due to the breathing modes of six-atom rings and requires a defect for its activation<sup>30</sup>. Typically in few-layer graphene dispersions, the D peak corresponds to flake edges rather than defects within the flakes' basal plane<sup>31,32</sup>. The 2D peak located at  $\sim 2700 \text{ cm}^{-1}$  is the second-order resonance of the D peak<sup>33</sup>. In the graphite sample (black curve), the 2D peak split into several components. As the number of layers decreases, the 2D peak

narrows to a single Lorentzian for single-layer graphene. For 2000 cycles, we observe a shoulder on the 2D peak ( $\sim 2690 \text{ cm}^{-1}$ ) indicating the presence of multilayer graphene. However, after 4000 and 6000 cycles, the 2D peak is a single Lorentzian fit, indicating that even if the flakes are multilayers, they are electronically decoupled and behave as a collection of single layers<sup>33</sup>. In disordered carbon, the position of the G peak,  $\text{Pos}(G)$  increases when the excitation wavelength,  $\lambda_L$  decreases from the IR to UV<sup>30,34</sup>. Additionally, the dispersion of the G peak,  $\text{Disp}(G) = \Delta\text{Pos}(G)/\Delta\lambda_L$  and the FWHM of the G peak,  $\text{FWHM}(G)$ , increase with disorder<sup>35,36</sup>. Combining the intensity ratio of the D and G peaks,

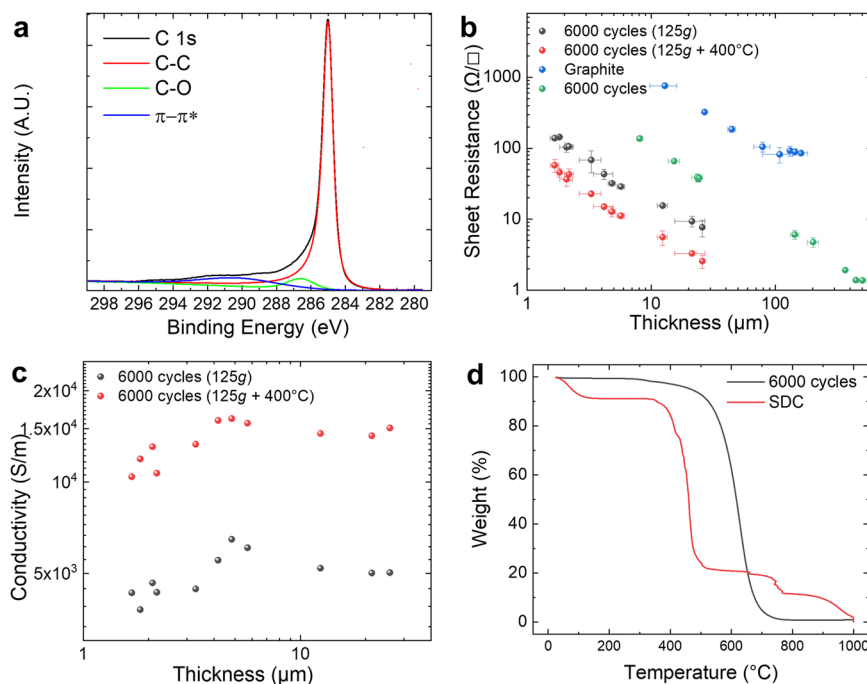


**Fig. 4 Chemical, electrical and thermal analysis of graphene inks.** **a** XPS C 1s spectra of the 6000 cycles graphene ink. **b** A plot of  $R_s$  as a function of the graphene and graphite film thickness for the 6000 cycles graphene ink with different post-processing conditions such as centrifugation and annealing. Error is calculated by standard deviation of mean (SDOM,  $n = 3$ ). **c** A graph of the  $\sigma$  as a function of thickness for the 6000 cycles graphene ink with post-processing. **d** Thermogravimetric analysis is used to find thermograms of the graphene powder and SDC surfactant. The weight change is plotted as a function of temperature.

$I(D)/I(G)$ , with  $\text{FWHM}(G)$  and  $\text{Disp}(G)$  can discriminate between disorder localised at the edges and disorder in the basal plane of the flakes. If the disorder is in the graphene basal plane,  $I(D)/I(G)$  will increase with  $\text{FWHM}(G)$  and  $\text{Disp}(G)$ . In the former case,  $I(D)/I(G)$  will be uncorrelated with  $\text{FWHM}(G)$  and  $\text{Disp}(G)$ . In Fig. 3b we find that  $I(D)/I(G)$  is uncorrelated with  $\text{Disp}(G)$ . Therefore, the D peak originates from the flake edges rather than the basal plane. Furthermore, the average  $\text{Disp}(G) \sim 0.019 \text{ cm}^{-1} \text{ nm}^{-1}$ , which is significantly lower than the  $\text{Disp}(G)$  for disordered carbons ( $>0.1 \text{ cm}^{-1} \text{ nm}^{-1}$ )<sup>34,37</sup>. Therefore, the in-line shear mixing method produces pristine basal plane graphene flakes. In Fig. 3c,  $I(D)/I(G)$  is plotted as a function of  $\text{FWHM}(G)$ . We find the  $\text{FWHM}$  is  $20 \pm 1 \text{ cm}^{-1}$  for each sample, indicating that the  $\text{sp}^2$  grain size ( $L_a$ )  $\sim 40 \text{ nm}$  remains constant before and after exfoliation and that the cyclic process does not significantly damage the graphene<sup>35,37</sup>. Since the D peak originates from the edge of the flakes and  $\text{FWHM}(G)$  remains constant in our samples, the  $I(D)/I(G)$  ratio can be used to determine  $\langle L \rangle$ , where  $I(D)/I(G)$  increases as a function of inverse  $\langle L \rangle$ <sup>18,38</sup>. In Fig. 3c, the  $I(D)/I(G)$  ratio increases with processing time from  $I(D)/I(G) \sim 0.1$  for bulk graphite (black),  $I(D)/I(G) \sim 0.25$  after 2000 cycles (red) and up to  $I(D)/I(G) \sim 0.5$  after 4000 (blue) and 6000 (green) processing cycles. We attribute the increase in  $I(D)/I(G)$  with processing time to a decrease in flake lateral size. We can estimate  $\langle L \rangle$  using the formula  $I(D)/I(G) \approx (I(D)/I(G))_{\text{graphite}} + k/\langle L \rangle$ , where  $k$  is the slope of  $I(D)/I(G)$  as a function of  $\langle L \rangle^{-1}$  measured by transmission electron microscopy<sup>18</sup>. Using  $I(D)/I(G) \sim 0.5$  for 4000 and 6000 cycles, average  $I(D)/I(G) \sim 0.11$  for our graphite and a slope of  $k = 0.17$  we can estimate that  $\langle L \rangle \sim 0.43 \mu\text{m}$  which is consistent with the SEM and AFM data<sup>18</sup>. In contrast, a correlation between  $I(D)/I(G)$  and  $\text{FWHM}(G)$  is observed with a graphene ink made by conventional shear mixing in a beaker under similar exfoliation parameters (Supplementary Note 1) indicating that in-plane defects are present where  $L_a \sim 20 \text{ nm}$ , which will decrease graphene conductivity. We attribute the introduction of in-plane defects to an increased Reynolds number ( $Re_{\text{beaker}} = \rho v L \eta^{-1} \sim 1.3 \times 10^6$ ) compared to our in-line shear

mixing process ( $Re_{\text{inline}} \sim 6 \times 10^5$ ), where  $\rho$  is the liquid density,  $v$  is the liquid velocity,  $L$  is the characteristic length and  $\eta$  is the liquid viscosity. The reduced  $Re_{\text{inline}}$  is attributed to the decreased  $L$  of the in-line shear mixing system  $L_{\text{inline}} \simeq 0.46 L_{\text{beaker}}$  (Supplementary Note 2) and suggests that reducing the turbulence of the system reduces the defects present in graphene flakes produced by shear mixing. Therefore, in-line shear mixing could offer a route to manufacture higher quality graphene material than is traditionally produced by shear mixing.

#### Investigating flake chemical, electrical and thermal properties

We use X-ray photoelectron spectroscopy (XPS) analysis to investigate the oxygen and sodium content in the 6000 cycles graphene ink. The XPS survey spectra (Supplementary Fig. 3a) shows very high carbon content ( $92.5 \pm 0.1 \text{ at.}\%$ ) and low oxygen content ( $5.7 \pm 0.1 \text{ at.}\%$ ), attributed primarily to graphene flakes and sodium content ( $\sim 1.8 \text{ at.}\%$ ), which we attribute to residual surfactant. The relatively low oxygen content and the position of the main peak in O 1s spectra at  $\sim 533 \text{ eV}$  (Supplementary Fig. 3b) suggest C-O component dominance over C=O. Careful investigation of the high-resolution XPS spectra (Fig. 4a) for carbon 1s reveals a peak at  $\sim 285 \text{ eV}$  attributed to the  $\text{sp}^2$  carbon component and indicative of the hexagonal lattice structure, also the satellite peak ( $\pi-\pi^*$ ) contribution, corresponding to the broad peak at  $\sim 290 \text{ eV}$ , is a characteristic feature of  $\text{sp}^2$  hybridisation of carbon<sup>39</sup>. The  $\pi-\pi^*$  transition occurs due to the delocalisation of the  $\pi$ -electrons in the carbon aromatic ring<sup>40</sup>. We observe that the  $\pi-\pi^*$  peak is more pronounced in the 6000 cycles graphene ink than conventional shear mixing in a beaker (Supplementary Fig. 3), suggesting that 6000 cycles graphene ink should have reduced basal plane defects. In general, the more pronounced  $\pi-\pi^*$  satellite peak, the greater the degree of  $\text{sp}^2$  bonding<sup>41</sup>.

To examine the graphene inks' electrical properties, we create films of the 6000 cycles graphene ink and graphite flakes by drop-casting onto glass slides with a spacer to control the wet film

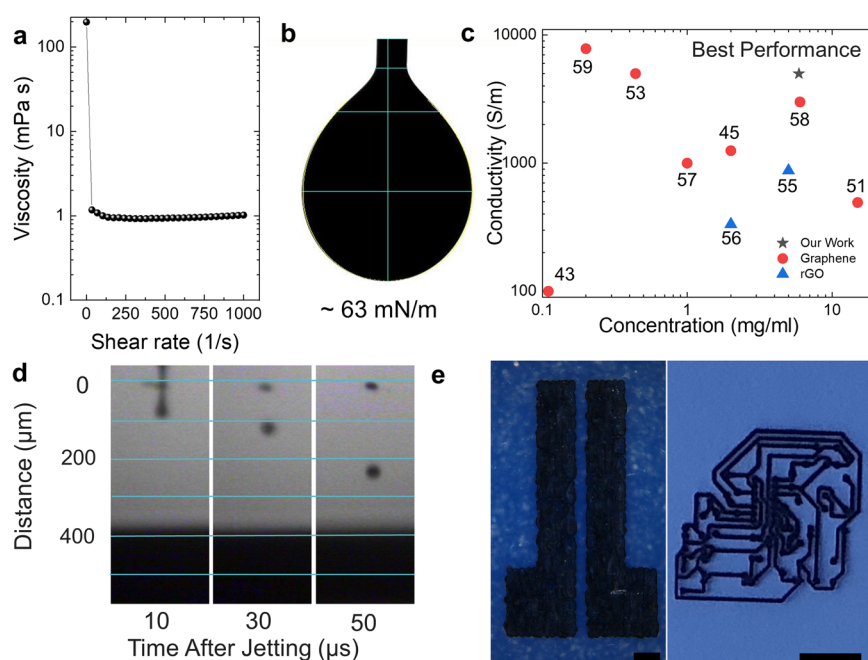


**Fig. 5 Inkjet printed interconnects and electrodes.** **a** Ink viscosity as a function of applied shear rate, demonstrating non-Newtonian shear thinning behaviour. **b** Pendant drop of the ink used to calculate the surface tension. **c** Literature review of other inkjet printable conductive inks comparing their  $\sigma$  with the ink **c**. **d** Jetting of the ink observed with a stroboscopic camera. **e** Optical image of the inkjet-printed transistor contacts (left, dark field) and interconnect (right, bright field). The scale bar is 100  $\mu\text{m}$  (left) and 1 cm (right).

thickness. The films are dried at  $\sim 100^\circ\text{C}$  on a hotplate to remove excess water. The dry film thickness ( $t$ ) depends on the  $c$  of the ink and wet film thickness. Therefore, we vary  $t$  by increasing the number of droplets cast (e.g. 5 to 50) from a syringe. We find the sheet resistance ( $R_s$ ) of each sample using a four-point probe (Jandel Probe) in three different locations to obtain an average. We use a profilometer to determine  $t$  for each sample and measure three areas to obtain an average. In Fig. 4b, we find a  $R_s$  of  $\sim 324 \Omega \square^{-1}$  for the graphite film at  $t \sim 27 \mu\text{m}$ . Consequently, the conductivity ( $\sigma$ ) can be estimated using  $\sigma^{-1} = R_s t$ , equating to  $\sigma \sim 100 \text{ S m}^{-1}$ . Without any post-processing or centrifugation, we find that the 6000 cycles graphene ink has an  $R_s$  of  $\sim 37 \Omega \square^{-1}$  at  $t \sim 24 \mu\text{m}$ , corresponding to  $\sigma \sim 1.1 \times 10^3 \text{ S m}^{-1}$ , one order of magnitude higher than  $\sigma$  of graphite, indicating graphite's exfoliation to few-layer graphene. Recently, Fernandes et al. has determined through semi-automated AFM measurements that uncentrifuged graphene LPE dispersions could have a small number ( $\sim 5\%$ ) of graphite flakes, and the majority mass ( $\sim 90\%$ ) would be attributed to the thicker ( $>40 \text{ nm}$ ) material<sup>42</sup>. Therefore, we centrifuge the material at low speed (1k rpm,  $g \sim 125$ ) to remove the small number of thicker flakes ( $>40 \text{ nm}$ ), and the film  $\sigma$  increases to  $\sim 5 \times 10^3 \text{ S m}^{-1}$ . We show the  $\sigma$  as a function of  $t$  in Fig. 4c. At  $t < 4 \mu\text{m}$ , the  $\sigma$  is thickness dependant, and at  $t \sim 4 \mu\text{m}$ , the flakes form a percolative network, and the bulk  $\sigma$  is reached. Therefore, for electronic devices requiring high conductivity  $>10^3 \text{ S m}^{-1}$  a  $t$  of at least  $4 \mu\text{m}$  should be used. The residual surfactant can degrade the electrical properties of a deposited network of flakes<sup>43</sup>. Therefore, we then anneal the samples at  $400^\circ\text{C}$  for 30 min to combust the SDC used in the graphene ink. We find  $\sigma$  increases even further to  $\sim 1.5 \times 10^4 \text{ S m}^{-1}$  and demonstrates  $R_s \sim 2.6 \Omega \square^{-1}$  ( $t \sim 25 \mu\text{m}$ ). The  $\sigma$  of the film is comparable to state-of-the-art printable graphene inks<sup>20,44,45</sup>. To investigate the removal of residual SDC surfactant after annealing, we investigate the SDC decomposition temperature with thermogravimetric analysis (TGA) in Fig. 4d. The 6000 cycles graphene ink is subjected to a freeze-drying process to obtain a graphene powder (see Methods). The SDC and graphene powder are heated from  $\sim 25^\circ\text{C}$  up to  $1000^\circ\text{C}$  ramped at a rate of  $\sim 10^\circ\text{C min}^{-1}$  in an

air atmosphere. We plot the weight change as a function of temperature, which shows that SDC significantly decomposes at temperatures  $>380^\circ\text{C}$ . The graphene powder has a carbon combustion temperature between  $570$  and  $670^\circ\text{C}$  (maximum mass decomposition rate  $\approx 627^\circ\text{C}$ ), which is associated with the carbon decomposition temperature of few-layer graphene<sup>46</sup>.

### Inkjet printable interconnects

To make an inkjet printable ink requires the optimisation of  $c$ , surface tension,  $\gamma$  and  $\eta$  to ensure satellite droplet free ejection, and morphologically uniform (i.e. roughness minimisation) printed films<sup>43,47</sup>. We engineer the  $\eta$  of the graphene ink to ensure it is within an optimal  $1\text{--}10 \text{ mPa s}$  range required for inkjet printing<sup>43</sup>. We measure  $\eta$  with a parallel plate rotational rheometer (see Methods). A known shear rate is applied, and the resultant torque or shear stress is measured. The shear stress divided by the shear rate calculates the liquid viscosity shown in Fig. 5a<sup>43</sup>. We find pseudoplastic behaviour with an infinite-rate  $\eta$  of  $\sim 1 \text{ mPa s}$  within the optimal  $\eta$  range ( $\sim 1\text{--}10 \text{ mPa}$ )<sup>43</sup>. The decrease in viscosity is attributed to the reduction in the Brownian motion of the graphene flakes<sup>48</sup>. In Fig. 5b, we determine the ink  $\gamma$  using the pendant drop method. The pendant drop method involves using a camera to visualise the shadow image of a droplet dispensed from a needle. The droplet's radius of curvature is found from the shadow images that can be used with the Young-Laplace equation to determine the liquid surface tension<sup>49,50</sup>. We find a graphene ink  $\gamma$  of  $\sim 63 \text{ mN m}^{-1}$ , lower than the  $\gamma$  of water  $\sim 72 \text{ mN m}^{-1}$ , which we attribute to the presence of SDC surfactant. High  $c$  is needed to minimise the number of printing layers required to reach a thick network of flakes, thus increasing the  $\phi$  of a printing process to create devices. In contrast, high  $\sigma$  is desirable to improve the performances of devices that require high  $\sigma$ , such as electrodes for micro-supercapacitors<sup>51</sup>, antennas<sup>52</sup> or transistor electrodes<sup>53</sup>. Pristine inkjet printable graphene inks have commonly had low  $c$  ( $< 3 \text{ mg ml}^{-1}$ ), to help minimise nozzle clogging. Identification of stabilising solvents by solubility parameter-matching<sup>16</sup> has proven to be a useful starting point

6 for ink formulation. However, the resultant  $c$  can be low,  $< 0.2 \text{ mg ml}^{-1}$ <sup>44</sup>; therefore, many ( $>50$ ) printing passes are required to build a percolating film of material. Other strategies have been developed to improve ink's  $c$ . For example, vacuum filtration can be utilised with flocculation agents<sup>51</sup> or a solvent exchange<sup>53</sup> to redisperse graphene at high  $c$  ( $> 10 \text{ mg ml}^{-1}$ ). However, the additional vacuum filtration step reduces  $\phi < 1 \text{ g h}^{-1}$ <sup>53</sup>. Alternately solvent interface trapping has been used engineer high  $c$  ( $> 100 \text{ mg ml}^{-1}$ ) ink by trapping graphene between a polar and non-polar solvents<sup>54</sup>. GO powders also been used to directly disperse material at a high ( $> 1 \text{ mg ml}^{-1}$ )  $c$  but with low  $\sigma$  ( $< 1000 \text{ S m}^{-1}$ ) due to the defective nature of the flakes<sup>55,56</sup>. To increase the  $\sigma$ , printed films are typically annealed at high temperatures  $>300^\circ\text{C}$ <sup>45,57</sup>. However, this process is incompatible with many textile (e.g. cotton) or polymer (e.g. polyethylene terephthalate, PET) substrates which degrade at temperatures  $>100^\circ\text{C}$ <sup>43</sup>. Therefore inkjet printable graphene inks with high  $\sigma$  ( $> 10^3 \text{ S m}^{-1}$ ) and high  $c$  ( $> 10 \text{ mg ml}^{-1}$ ), which do not clog the inkjet nozzle have been desirable but difficult to achieve. The 6000 cycles graphene ink achieves these requirements ( $\sigma > 10^3 \text{ S m}^{-1}$ ,  $c \sim 100 \text{ mg ml}^{-1}$ ), however it is not compatible with most inkjet nozzles due to the flake  $\langle L \rangle > 1 \mu\text{m}$ . Typically the flakes should be 1/50th of the nozzle diameter ( $a = 21 \mu\text{m}$ ) to minimise nozzle clogging ( $\sim 420 \text{ nm}$ )<sup>44</sup>. Therefore we centrifuge the 6000 cycles graphene ink at low speed (1k rpm,  $g \sim 125$ ) to create a graphene ink  $G_{\text{inkjet}}$  with  $c \sim 5.9 \text{ mg ml}^{-1}$ , ( $Y_w \sim 6\%$ ) which minimises the probability of nozzle clogging and increases  $\sigma \sim 5 \times 10^3 \text{ S m}^{-1}$  without annealing. We compare the  $\sigma$  and  $c$  of  $G_{\text{inkjet}}$  to others (Fig. 5c) and find that both  $c$  and  $\sigma$  are higher than most inkjet printable inks in the literature, where an optimal ink would be in the top right corner of the graph, assuming that the ink would not cause nozzle clogging issues or satellite droplets due to its concentration<sup>44,45,51,53,55-59</sup>. We use a drop-on-demand inkjet printer to print the ink. We image the jetting of the ink with a stroboscopic camera (Fig. 5d), the black dot at  $0 \mu\text{m}$  represents the inkjet nozzle. The ink is observed to eject from the nozzle without satellite droplets, which is important to achieve well resolved printed films with resolution  $< 100 \mu\text{m}$ . In Fig. 5e, we deposit the ink onto a PET substrate coated with aluminium oxide nanoparticles (Novel, Novacentrix) which have a low roughness ( $\sim 18 \text{ nm}$ ). We print a  $2 \text{ cm}^2$  layout of interconnect array. Through optical inspection, we observe morphological uniformity of the print and evenly distributed flakes in the form of a film. We also inkjet print transistor contacts Fig. 5e demonstrating a  $\sim 50 \mu\text{m}$  gap between two graphene electrodes. The resolution of  $\sim 50 \mu\text{m}$  is as expected and comparable to previous works on inkjet printing<sup>47,53</sup>. These results indicate that the high concentration ( $5.9 \text{ mg ml}^{-1}$ ) printable graphene inks can be produced using in-line shear mixing and can be inkjet printed at high resolution ( $\sim 50 \mu\text{m}$ ) in desirable patterns for flexible electronics.

### Li-ion battery anode

Graphene is an attractive material to replace graphite in lithium-ion battery anodes since Li-ion battery anodes need high in-plane conductivity ( $> 10^3 \text{ S m}^{-1}$ ) to improve rate performance, and thus, charging speed<sup>60,61</sup>. Here, we demonstrate the potential of the graphene flakes produced using in-line shear mixing method as Li-ion anodes. Rather than using a polymeric binder, we add a small amount (15%) of single-walled carbon nanotubes (SWCNT) to the electrode. Using SWCNT is known to simultaneously maximise the electrode's mechanical and electrical properties and tends to yield electrodes that perform near their theoretical capability<sup>62</sup>. The resultant graphene/SWCNT anodes have an active mass loading of  $\sim 1 \text{ mg cm}^{-2}$  combined with a SWCNT loading of  $\sim 0.18 \text{ mg cm}^{-2}$  and thickness of  $\sim 20 \mu\text{m}$  (see Methods).

To evaluate the electrochemical Li storage mechanism of graphene produced using in-line method, cyclic voltammetry

(CV) data is measured for a graphene/SWCNT anode at a scanning rate of  $0.1 \text{ mV s}^{-1}$ , shown in Fig. 6a. During the 1<sup>st</sup> cycle, an irreversible cathodic peak at  $\sim 1 \text{ V}$  is observed, which can be attributed to the formation of a solid electrolyte interface (SEI) and the reaction of lithium ions with residual oxygen-containing functional groups on the graphene flakes<sup>63-66</sup>. In the range of  $0.01\text{--}0.25 \text{ V}$ , we observe  $\text{Li}^+$  insertion into graphene flakes<sup>67</sup>. In the second cycle, the cathodic peak at  $1 \text{ V}$  is not observed, indicating the oxygen-containing functional groups on the graphene flakes are completely reduced. After five cycles, the redox peaks between  $0.01$  and  $0.25 \text{ V}$  display no apparent changes, illustrating reversible  $\text{Li}^+$  intercalation/deintercalation in the graphene layer. Thus, the CV data confirms that the 6000 cycles graphene flakes store lithium effectively<sup>68</sup>.

For cyclability measurement, the galvanostatic charge and discharge are performed initially with a 43-cycle of activation at  $30 \text{ mA g}^{-1}$  followed by 375 cycles at  $100 \text{ mA g}^{-1}$ , as shown in Fig. 6b. All data is normalised to the active mass of graphene (see Methods). The first activation cycle ( $30 \text{ mA g}^{-1}$ ) specific capacity ( $C_{\text{sp}}$ ) was  $\sim 646 \text{ mAh g}^{-1}$  for discharge and  $\sim 363 \text{ mAh g}^{-1}$  for charge, with an initial coulomb efficiency (CE) of  $\sim 56\%$ . After the activation cycles, the cells are tested for 375 cycles at  $100 \text{ mA g}^{-1}$ . The graphene/SWCNT anodes show a lithium storage capability of  $\sim 228 \text{ mAh g}^{-1}$  and  $\sim 243 \text{ mAh g}^{-1}$  for discharge and charge, with a CE of  $\sim 100\%$  for the first cycle at  $\sim 100 \text{ mA g}^{-1}$  (Fig. 6b, inset). The charging and discharging capacity changed in the first 4 cycles before stabilising at a capacity of  $\sim 233 \text{ mAh g}^{-1}$  for both discharge and charge with a CE of  $\sim 100\%$  over 365 cycles.

The rate performance of our anodes is tested with voltage profiles shown in Fig. 6c and rate dependent cycling data in Fig. 6d. The anodes exhibited an initial performance of  $641 \text{ mAh g}^{-1}$  for discharge and  $376 \text{ mAh g}^{-1}$  for first cycle charge at  $10 \text{ mA g}^{-1}$  with an initial CE of  $\sim 58.6\%$  that approaches  $\sim 99\%$  for subsequent cycles. The specific charge capacity decreased with increasing specific currents whereby at  $180 \text{ mA g}^{-1}$ , a specific charge capacity of  $\sim 107 \text{ mAh g}^{-1}$  was achieved. In contrast, the specific discharge capacities fell off to 374, 287, 197 and  $116 \text{ mAh g}^{-1}$  for each rate's first cycle, respectively. The low-rate capacity ( $20 \text{ mA g}^{-1}$ ) was  $\sim 370 \text{ mAh g}^{-1}$ , very close to graphite's theoretical capacity ( $372 \text{ mAh g}^{-1}$ )<sup>69</sup>. The fact that we can reach close to the theoretical value attests to the high quality of graphene flakes produced using in-line method while facilitated by the presence of SWCNT<sup>60,62</sup>.

### Biocompatibility with human cells

Understanding the biocompatibility of the graphene flakes with human cells is essential to utilise the material for applications that come into contact with humans, such as electronic textiles, bioscaffolds or drug delivery<sup>9,70,71</sup>. To test if there is any acute toxicity, we performed viability assays using increasing graphene flake concentrations (6000 cycles graphene ink) in Human umbilical vein endothelial cell (HUVECs) and standard human cancer cell line SW948. In Fig. 7a, the upper left quadrant represents acute toxicity by induction of cell necrosis stained by 7-AAD. In contrast, the lower right quadrant shows cells undergoing programmed cell death (Annexin V staining), i.e. apoptosis. Cells stained by both dyes are in a transitional phase between apoptosis and necrosis and fall in the right upper quadrant. Repeated measurements show no acute toxicity found when using the highest concentration of graphene ( $1 \text{ mg ml}^{-1}$ ) in 48 h cell culture treatments ( $N = 2$  for SW948,  $N = 3$  for HUVECs). This was comparable to a control, where no graphene was added.

To confirm our cellular apoptotic measurements, we used a cell counting kit-8 (CCK8) assay based on a tetrazolium salt reduced by viable cells to a soluble formazan dye. The resulting dye absorbs light at  $450 \text{ nm}$ , which correlates with cellular viability (Fig. 7b). After 48 h of graphene treatment, the cell cultures did not show

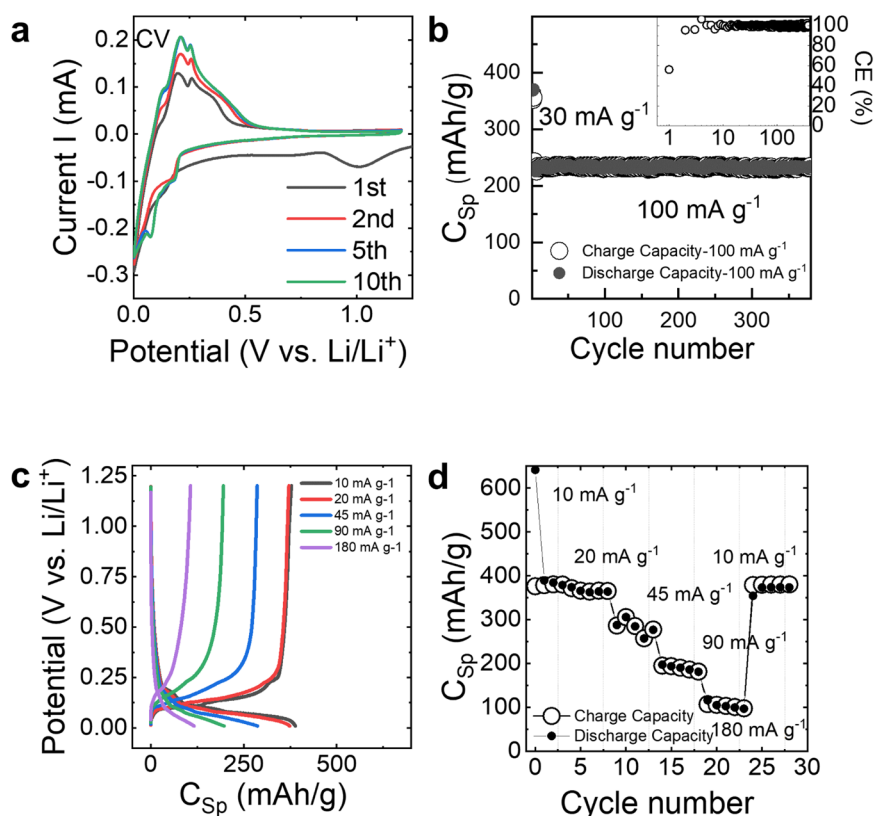


**Fig. 6** Li-ion battery performance: performance of graphene flakes/SWCNT (85:15 wt%) as lithium-ion battery anodes. **a** Cyclic voltammograms at a scan rate of  $0.1 \text{ mV s}^{-1}$  for various cycles. **b** Cycling capacity versus cycle number for composite anodes based on graphene flakes cycled initially at  $30 \text{ mA g}^{-1}$  and then at  $100 \text{ mA g}^{-1}$ . Coulombic efficiency (CE) is shown in the inset. **c** Galvanostatic charge-discharge curves measured at different charging currents. **d** Specific capacity as a function of charging current. In all cases,  $C_{Sp}$  is normalised to the graphene mass.

any dose-dependent toxicity up to the highest concentration tested at  $1 \text{ mg ml}^{-1}$  for SW948 and no significant toxicity up to  $500 \text{ } \mu\text{g ml}^{-1}$  for HUVECs. We compared our measurements against a control of deionised water and SDC, which did not show any dose-dependent toxicity up to  $38.46 \text{ } \mu\text{g ml}^{-1}$  of SDC (relative to the amounts contained in  $1 \text{ mg ml}^{-1}$  graphene suspension, Supplementary Fig. 4). To the best of our knowledge, this is one of the highest  $c$  that has demonstrated LPE graphene's biocompatibility with human cells to date, which is essential for applications in printed electronics that use  $c$  of at least  $1 \text{ mg ml}^{-1}$ .<sup>43</sup> We attribute the biocompatibility on the ink to the lack of oxygen functional groups ( $\sim 5.7\%$ , determined by XPS) as graphene oxide dispersions have previously demonstrated toxicity to human cells as low as  $1\text{--}10 \text{ } \mu\text{g ml}^{-1}$ .<sup>72,73</sup> attributed to its high oxygen content ( $\sim 47\%$ ) that induces the formation of reactive oxygen species that can be toxic to cells<sup>74</sup>. To detect any cell deformities due to graphene treatment, we imaged the cells using laser scanning confocal microscopy with propidium iodide to stain whole fixed cells with the nuclear Hoechst dye (Fig. 7c). Representative images show cells with similar morphology to control at high graphene treatments (Fig. 7c).

## DISCUSSION

We demonstrated an enclosed, cyclic exfoliation of graphene with in-line shear-mixing, which has a higher  $\phi \sim 8.3 \text{ g h}^{-1}$  than previous graphene production techniques such as ultrasonication and ball milling. The  $Y_w \sim 100\%$  is several orders of magnitude increase compared to previous work on shear mixing<sup>18</sup>, and can be used to create dispersions with extremely high concentration  $c \sim 100 \text{ mg ml}^{-1}$ , achieving  $\sigma \sim 10^3 \text{ S m}^{-1}$  without post-processing

and  $\sigma \sim 1.5 \times 10^4 \text{ S m}^{-1}$  after centrifugation and annealing, which is state of the art for graphene inks. We achieve high  $\sigma$  by reducing  $\text{Re} < 10^6$  which minimises basal plane topological defects. Therefore, in-line shear mixing could offer a route to manufacture higher quality graphene or potentially other 2D materials, than is traditionally produced by shear mixing. We demonstrate the graphene inks' versatility by making anode electrodes with SWCNTs for Li-ion energy storage, achieving a low-rate capacity of  $\sim 370 \text{ mAh g}^{-1}$ . We show that highly concentrated ( $5.9 \text{ mg ml}^{-1}$ ) and inkjet printable inks can be manufactured for use in inkjet-printed conductive interconnects with a resolution  $\sim 50 \text{ } \mu\text{m}$ . As a final demonstration, we examine the toxicity of the graphene flakes with human colon cells and HUVEC cells. We observe no dose-dependent toxicity up to 48 h indicating the graphene flakes' biocompatibility at high concentrations  $\sim 1 \text{ mg ml}^{-1}$ , which is essential to utilise graphene in textile electronics, composites and printed interconnects that could involve human contact with high concentrations of graphene.

## METHODS

### Inkjet printing

We used a Fujifilm Dimatix DMP-2800 inkjet printer with a  $21 \text{ } \mu\text{m}$  diameter nozzle (Fujifilm DMC-11610) for the printing of interconnects. The inkjet printing platen temperature was kept at ambient conditions ( $20 \text{ } ^\circ\text{C}$ ). An inter-drop spacing of  $25 \text{ } \mu\text{m}$  was used for the interconnects and an inter-drop spacing of  $40 \text{ } \mu\text{m}$  for the transistor electrodes. We print 100 layers of ink to construct the interconnect pattern and 10 layers of ink for the transistor electrodes. We used a maximum jetting frequency of  $2 \text{ kHz}$ .

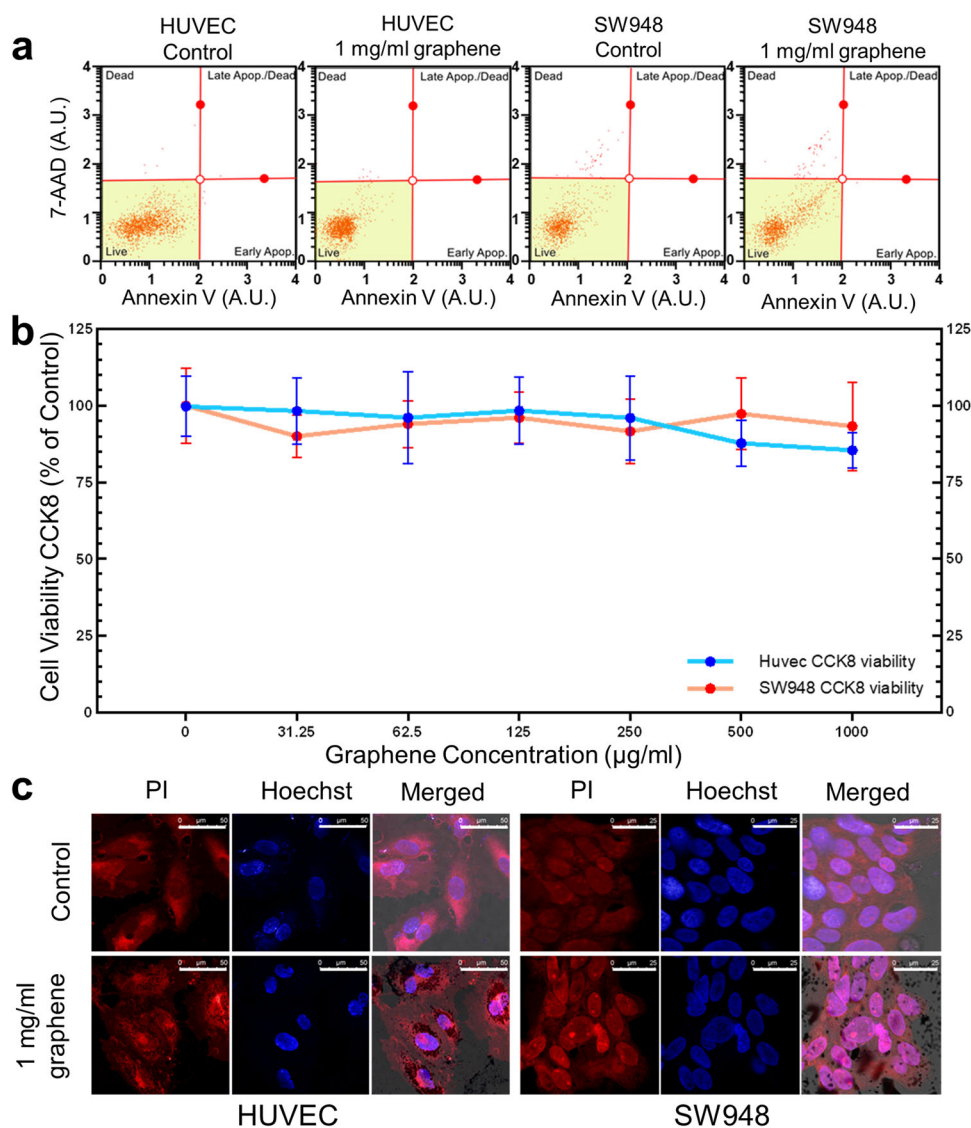


**Fig. 7 Human cell viability study: biocompatibility with human umbilical vein endothelial cell (HUVECs) and SW948 human cells.** **a** Muse™ Apoptotic profile using Annexin V for apoptosis staining and 7-Aminoactinomycin D (7-AAD) fluorescence intensity for necrosis is shown in a flow scatter using same cut offs for all measurements ( $N = 3$  for HUVECs and  $N = 2$  for SW948). **b** CCK8 viability normalised to  $0 \mu\text{g ml}^{-1}$  control over increasing concentrations of graphene ( $0$ – $1000 \mu\text{g ml}^{-1}$ ) ( $N = 9$  from three independent experiments for HUVECs in blue and  $N = 6$ , from two independent experiments for SW948 in red). **c** Laser scanning confocal microscopy with the addition of propidium iodide (PI), used here to image whole cells, and image overlay with Hoechst cell nuclear staining with bright field transmittance of graphene pre-treated fixed cells at  $\times 63$  magnification, scale bar  $50 \mu\text{m}$  for HUVECs and  $25 \mu\text{m}$  for SW948 cells.

### X-ray diffraction

XRD patterns were recorded with a D2 Phaser (Bruker) powder diffractometer equipped with LynxEye detector using Cu K $\alpha$  radiation ( $\lambda = 1.54 \text{ \AA}$ ) at a  $2\theta$  scan step of  $0.03^\circ$  and 1 s dwell time. XRD samples were prepared by drying the graphene dispersions under room condition and transferring the powder obtained to the Bruker sample holder.

### X-ray photoelectron spectroscopy

Samples were prepared by depositing graphene dispersions on Si/SiO<sub>2</sub> substrates mounted on aluminium stubs using conductive silver paint. XPS measurements were conducted using a K-Alpha™ X-ray Photoelectron Spectrometer (Thermo Scientific). High-resolution C1s, O 1s, and Na 1s spectra were collected at 40 eV pass energy with a 0.05 eV step size. Spectra were acquired using a monochromatic Al K $\alpha$  X-ray ( $h\nu = 1486.6 \text{ eV}$ ) with an X-ray beam spot size of  $400 \mu\text{m}$ , average of 3 points per sample were taken. Any energy shifts were calibrated using gold foil attached to the films and measuring the Au 4f binding energy at 84 eV as a standard.

The XPS measurement data were analysed using the CasaXPS software (Casa Software Ltd).

### Profilometry

We used a stylus profilometer (Bruker DektakXT) to measure the thickness of the deposited films on a quartz substrate. A stylus force of 3 mg was used with a tip of radius  $12.5 \mu\text{m}$  over the sample.

### Thermogravimetric analysis

To prepare the graphene sample, we take 30 ml of the 6000 cycles graphene ink and froze it at  $-18^\circ\text{C}$ . The frozen sample was then placed inside a freeze dryer (Telstar LyoQuest) to remove ice crystal by sublimation under vacuum overnight to make a graphene powder. We then undertake thermal analysis of the graphene powder and SDC surfactant using a thermogravimetric analyser (TA Instruments Q50) in air with a ramping temperature of  $10^\circ\text{C min}^{-1}$  from  $\sim 25^\circ\text{C}$  up to  $1000^\circ\text{C}$ .



### Raman spectroscopy

We acquired the Raman spectra at 514.5 nm with a Reinshaw InVia equipped with a 50× objective. We kept the power on the samples below ~1 mW to minimise thermal damage from the laser. About 20 spectra are taken for each map. All measurements are acquired after drop-casting sample solution on Si/SiO<sub>2</sub> wafer. The resolution of our spectrometer is ~1 cm<sup>-1</sup> and our spot size was ~2 μm. For measurement of the Disp(G) we acquired additional Raman spectra at 457 nm and 633 nm, respectively.

### Shear-mixing and ink preparation

We used a Silverson Model L5M, 250 W single phase motor high-shear laboratory mixer. An interchangeable in-line mixing assembly was used for in-line processing. It was equipped with a 4-blade rotor placed inside a stator with a rotor-stator gap ( $\Delta R$ ) of 300 μm and a rotor diameter ( $D$ ) of 31.1 mm. We use graphite flakes (Imerys Graphite) as a starting material for the inks. We mix the flakes (100 mg ml<sup>-1</sup>) with sodium deoxycholate (SDC, 5 mg ml<sup>-1</sup>) (Sigma-Aldrich) in deionised water at 8000 rpm. The throughput was calculated as 1000 ml of 100 mg ml<sup>-1</sup> ink (i.e. 100 g) processed for 4000 cycles (i.e. 12 h). The volume of the ink reservoir can be increased (>1 L) if further scale is required. The shear rate  $\dot{\gamma} \approx \pi ND \Delta R^{-1} \approx 4 \times 10^4 \text{ s}^{-1}$ , where  $N$  is the revolutions per second of the shear mixer (8000 rpm = 133 s<sup>-1</sup>)<sup>18</sup>. Optical inspection of the ink reveals a homogeneous stable dispersion of graphene flakes.

### Scanning electron microscopy

The ink was diluted 1:999 and drop-cast on 1 cm<sup>2</sup> Si/SiO<sub>2</sub> wafer. We acquired scanning electron microscopy images with a Magellan 400 L SEM. We used an accelerating voltage of 5 kV and gun current of 25 pA during operation and obtained the images in secondary electron detection mode using an immersion lens and through-lens-detector. We measured  $\langle L \rangle$  in ImageJ.

### Atomic force microscopy

The ink was diluted 1:999 and drop-cast onto clean 1 cm<sup>2</sup> Si/SiO<sub>2</sub> wafers. We used a Bruker Dimension Icon in peakforce mode to scan a 20 μm × 20 μm area of the wafer. We then find the  $\langle L \rangle$  and thickness of 30 flakes by manual counting in NanoScope Analysis.

### Surface tension

We used a contact angle goniometer to measure the graphene ink's surface tension through the pendant drop method. A suspended droplet from a needle forms a pendant's shape resulting from the downward force due to gravity and the upward force due to surface tension. We used drop-shape analysis to calculate the surface tension from a shadow image of the droplet.

### Rheometry

We used a parallel-plate rotational rheometer (DHR Rheometer, TA instruments) to find the viscosity as a function of the shear rate. We use a plate-to-plate distance of 500 μm and we loaded the ink between the plates by capillary action at a gap of 550 μm. We find the infinite-rate viscosity for the ink.

### Microbalance

To find the  $c$  of the ink we use a microbalance (Sartorius ME5), we placed 1 ml of ink in a metal container and weighed the graphene flakes after evaporation of the solvent.

### Electrochemical characterization

The 6000 cycles graphene ink was mixed with a SWCNT aqueous dispersion (0.4 wt% SWCNT in water, ~0.6 wt% carboxymethyl cellulose (CMC) as a surfactant stabiliser, Tuball, OCSiAI), which increases conductivity and functions as a binder. A mortar and pestle ground the mixed solution to obtain a uniform slurry, and then the slurry was cast onto copper foil using a doctor blade. The slurry cast anodes were slowly dried at 40 °C overnight in an oven to remove residual water. The films produced were cut to the desired dimensions (area = 1.131 cm<sup>2</sup>) for electrochemical testing. The anodes were annealed at 700 °C for 2 h in a vacuum tube

furnace to remove CMC. The mass loading of graphene was ~1 mg cm<sup>-2</sup>, with 15 wt.% SWCNT. The anode thickness was ~20 μm.

Half-cell coin cells were assembled with Li-metal discs (diameter: 14 mm, MTI Corp.) as counter/reference electrodes. The electrolyte used was 1.2 M LiPF<sub>6</sub> in a mixture of ethylene carbonate/ethyl methyl carbonate (EC/EMC, 1:1 in v/v, BASF) with 10 wt% fluoroethylene carbonate (FEC). A Celgard 2320 (thickness 20 μm) was used as the separator. The cells were assembled in a glovebox filled with highly pure argon gas (UNIlab Pro, Mbraun, with O<sub>2</sub> and H<sub>2</sub>O levels <0.1 ppm).

### Cyclic voltammetry

Cyclic voltammetry of the cells was carried out using a galvanostat–potentiostat between 0.01 and 1.2 V vs. Li<sup>+</sup>/Li at a scan rate of 0.1 mV s<sup>-1</sup> for 10 cycles. For cycling capability tests, the cells were performed at 100 mA g<sup>-1</sup> for 375 cycles after 3 cycles activation at 30 mA g<sup>-1</sup>. For rate capability measurement, cells were running at different current rates of 10, 20, 45, 90, 180 mA g<sup>-1</sup> and then went back to 10 mA g<sup>-1</sup>. There are only 4 cycles at 10 mA g<sup>-1</sup>, then there are 5 cycles for the next steps at different current rates.

### Cell viability study

SW948 cells were seeded in 96 well plates at 15k cells per well in Dulbecco's Modified Eagle Medium (DMEM) media (5 mM glucose), with added 10% Foetal Bovine Serum (FBS), 5mM L-Glutamine (L-Glu), 5 mM penicillin (PC) and 5 mM streptomycin (SP), and left overnight in a humidified CO<sub>2</sub> infused incubator at 37 °C. Graphene ink was added to the wells to reach  $c$  ranging between 7.8 μg ml<sup>-1</sup> to 1000 μg ml<sup>-1</sup>. After 48 h, the cells were gently washed three times with PBS, where cells in one of the plates were resuspended in cell media (i.e. DMEM/glucose/FBS/L-Glu/PC/SP), containing 10% of the viability reagent cell counting kit 8 (CCK-8, Dojindo Molecular Technologies, Inc.). According to the assay protocol, one plate was incubated at 37 °C for 2 h before measuring absorbance at 450 nm using Spectramax Paradigm plate reader (Molecular Devices, Sunnyvale, CA 95134). After measuring absorbance, these wells were rewashed with phosphate-buffered saline (PS) at 0.01 M in deionised water, before another absorbance measurement was conducted at 450 nm to determine any background absorbance resulting from cellular internalised graphene, which was subsequently subtracted. An identical 96 well cell plate was fixed with 4% w/v paraformaldehyde (PFA) solution containing 15 μg ml<sup>-1</sup> Hoechst for 30 min, washed once with PBS, before Hoechst fluorescence was measured at 360nm<sup>Excitation</sup>/500nm<sup>Emission</sup> on a Spectramax Paradigm plate reader (Molecular Devices, Sunnyvale, CA 95134).

### Cell microscopy

Cells were imaged using Leica SP8 confocal microscope in epifluorescence mode for full well overviews and laser scanning confocal mode for high-resolution imaging.

### Muse™ flow cytometry viability and apoptosis assays

SW948 cells were seeded in sterile 24 well plates at 45k cells per well in cell culture media (complete DMEM), and left to attach in a humidified CO<sub>2</sub> infused incubator at 37 °C overnight. The next day, graphene ink was added to the cell growth media in each well to make a final  $c$  of 125, 250, 500, 1000 μg ml<sup>-1</sup> before being left for 48 h in the incubator as described above. Following 48-h treatment with graphene inks, cells were washed with pre-heated phosphate-buffered saline (PBS), and detached from culture wells using disodium ethylenediaminetetraacetic acid (EDTA) and 0.25% Trypsin (w/v%) (Thermo Fisher 25200056). 20 μL of cell suspension was added to 380 μL of count and viability Muse reagent and left for 5 min before measuring 1000 cellular event using Muse™ cell analyser. For apoptosis 100 μL of cell suspension was added to 100 μL of Muse<sup>®</sup> Annexin V & Dead Cell Reagent and left for 20 mins at room temperature before measuring 5000 cellular event using Muse™ cell analyser.

### DATA AVAILABILITY

The authors declare that the data supporting the findings of this study are available within the paper and its supplementary information files. Data are also available from the corresponding author upon reasonable request.

Received: 5 June 2021; Accepted: 1 December 2021;

Published online: 12 January 2022

## REFERENCES

- Kong, W. et al. Path towards graphene commercialization from lab to market. *Nat. Nanotechnol.* **14**, 927–938 (2019).
- Barkan, T. Graphene: the hype versus commercial reality. *Nat. Nanotechnol.* **14**, 904–906 (2019).
- Bohm, S. Graphene against corrosion. *Nat. Nanotechnol.* **9**, 741–742 (2014).
- Papageorgiou, D. G., Kinloch, I. A. & Young, R. J. Mechanical properties of graphene and graphene-based nanocomposites. *Prog. Mater. Sci.* **90**, 75–127 (2017).
- Carey, T., Jones, C., Le Moal, F., Deganello, D. & Torrisi, F. Spray-coating thin films on three-dimensional surfaces for a semitransparent capacitive-touch device. *ACS Appl. Mater. Interfaces* **10**, 19948–19956 (2018).
- Posen, I. D., Jaramillo, P., Landis, A. E. & Griffin, W. M. Greenhouse gas mitigation for U.S. plastics production: energy first, feedstocks later. *Environ. Res. Lett.* **12**, 034024 (2017).
- Moradi, B. & Botte, G. G. Recycling of graphite anodes for the next generation of lithium ion batteries. *J. Appl. Electrochem.* **46**, 123–148 (2016).
- Spasenovic, M. in *Graphene Technology* (eds Nazarpour, S. & Waite, S. R.) 177–187 (Wiley-VCH, 2016).
- Qiang, S. et al. Wearable solid-state capacitors based on two-dimensional material all-textile heterostructures. *Nanoscale* **11**, 9912–9919 (2019).
- Magdassi, S., Grouchko, M. & Kamyshny, A. Copper nanoparticles for printed electronics: routes towards achieving oxidation stability. *Materials (Basel)* **3**, 4626–4638 (2010).
- Karlsson, H. L., Cronholm, P., Gustafsson, J. & Möller, L. Copper oxide nanoparticles are highly toxic: a comparison between metal oxide nanoparticles and carbon nanotubes. *Chem. Res. Toxicol.* **21**, 1726–1732 (2008).
- Domanski, K. et al. Not All that glitters is gold: metal-migration-induced degradation in perovskite solar cells. *ACS Nano* **10**, 6306–6314 (2016).
- Hummers, W. S. & Offeman, R. E. Preparation of graphitic oxide. *J. Am. Chem. Soc.* **80**, 1339–1339 (1958).
- Mattevi, C. et al. Evolution of electrical, chemical, and structural properties of transparent and conducting chemically derived graphene thin films. *Adv. Funct. Mater.* **19**, 2577–2583 (2009).
- Ferrari, A. C. et al. Science and technology roadmap for graphene, related two-dimensional crystals, and hybrid systems. *Nanoscale* **7**, 4598–4810 (2015).
- Hernandez, Y. et al. High-yield production of graphene by liquid-phase exfoliation of graphite. *Nat. Nanotechnol.* **3**, 563–568 (2008).
- Yao, Y. et al. Large-scale production of two-dimensional nanosheets. *J. Mater. Chem.* **22**, 13494–13499 (2012).
- Paton, K. R. et al. Scalable production of large quantities of defect-free few-layer graphene by shear exfoliation in liquids. *Nat. Mater.* **13**, 624–630 (2014).
- Parvez, K. et al. Exfoliation of graphite into graphene in aqueous solutions of inorganic salts. *J. Am. Chem. Soc.* **136**, 6083–6091 (2014).
- Del Rio Castillo, A. E. et al. High-yield production of 2D crystals by wet-jet milling. *Mater. Horiz.* **5**, 890–904 (2018).
- Karagiannidis, P. G. et al. Microfluidization of graphite and formulation of graphene-based conductive inks. *ACS Nano* **11**, 2742–2755 (2017).
- Bonaccorso, F. et al. Production and processing of graphene and 2d crystals. *Mater. Today* **15**, 564–589 (2012).
- Dalal, M. H., Lee, C.-Y. & Wallace, G. G. Simultaneous anodic and cathodic exfoliation of graphite electrodes in an aqueous solution of inorganic salt. *Chem-ElectroChem* **8**, 3168–3173 (2021).
- Munuera, J. M. et al. Electrolytic exfoliation of graphite in water with multifunctional electrolytes: en route towards high quality, oxide-free graphene flakes. *Nanoscale* **8**, 2982–2998 (2016).
- Lotya, M. et al. Liquid phase production of graphene by exfoliation of graphite in surfactant/water solutions. *J. Am. Chem. Soc.* **131**, 3611–3620 (2009).
- Bracamonte, M. V., Lacconi, G. I., Urreta, S. E. & Foa Torres, L. E. F. On the nature of defects in liquid-phase exfoliated graphene. *J. Phys. Chem. C* **118**, 15455–15459 (2014).
- Backes, C. et al. Equipartition of energy defines the size–thickness relationship in liquid-exfoliated nanosheets. *ACS Nano* **13**, 7050–7061 (2019).
- Kouroupis-Agalou, K. et al. Fragmentation and exfoliation of 2-dimensional materials: a statistical approach. *Nanoscale* **6**, 5926–5933 (2014).
- Tuinstra, F. & Koenig, L. Raman spectrum of graphite. *J. Chem. Phys.* **53**, 1126–1130 (1970).
- Ferrari, A. C. & Robertson, J. Interpretation of Raman spectra of disordered and amorphous carbon. *Phys. Rev. B* **61**, 14095–14107 (2000).
- Casiraghi, C. et al. Raman spectroscopy of graphene edges. *Nano Lett.* **9**, 1433–1441 (2009).
- Bianchi, V. et al. Terahertz saturable absorbers from liquid phase exfoliation of graphite. *Nat. Commun.* **8**, 15763–15763 (2017).
- Ferrari, A. C. et al. Raman spectrum of graphene and graphene layers. *Phys. Rev. Lett.* **97**, 187401–187401 (2006).
- Ferrari, A. C. & Robertson, J. Resonant Raman spectroscopy of disordered, amorphous, and diamondlike carbon. *Phys. Rev. B* **64**, 075414–075414 (2001).
- Ferrari, A. C., Rodil, S. E. & Robertson, J. Interpretation of infrared and Raman spectra of amorphous carbon nitrides. *Phys. Rev. B* **67**, 155306 (2003).
- Cançado, L. G. et al. Quantifying defects in graphene via raman spectroscopy at different excitation energies. *Nano Lett.* **11**, 3190–3196 (2011).
- Ferrari, A. C. Diamond-like carbon for magnetic storage disks. *Surf. Coat. Technol.* **180–181**, 190–206 (2004).
- Khan, U., O'Neill, A., Lotya, M., De, S. & Coleman, J. N. High-concentration solvent exfoliation of graphene. *Small* **6**, 864–871 (2010).
- Al-Gaashani, R., Najjar, A., Zakaria, Y., Mansour, S. & Atieh, M. A. XPS and structural studies of high quality graphene oxide and reduced graphene oxide prepared by different chemical oxidation methods. *Ceram. Int.* **45**, 14439–14448 (2019).
- Hayes, W. I., Joseph, P., Mughal, M. Z. & Papakonstantinou, P. Production of reduced graphene oxide via hydrothermal reduction in an aqueous sulphuric acid suspension and its electrochemical behaviour. *J. Solid State Electrochem* **19**, 361–380 (2015).
- Kelemen, S. R., Rose, K. D. & Kwiatek, P. J. Carbon aromaticity based on XPS I to II\* signal intensity. *Appl. Surf. Sci.* **64**, 167–174 (1993).
- Fernandes, T. F. D. et al. A semi-automated general statistical treatment of graphene systems. *2D Mater.* **7**, 025045 (2020).
- Torrisi, F. & Carey, T. Graphene, related two-dimensional crystals and hybrid systems for printed and wearable electronics. *Nano Today* **23**, 73–96 (2018).
- Torrisi, F. et al. Inkjet-printed graphene electronics. *ACS Nano* **6**, 2992–3006 (2012).
- McManus, D. et al. Water-based and biocompatible 2D crystal inks for all-inkjet-printed heterostructures. *Nat. Nanotechnol.* **12**, 343–350 (2017).
- Farivar, F. et al. Unlocking thermogravimetric analysis (TGA) in the fight against “Fake graphene” materials. *Carbon* **179**, 505–513 (2021).
- Carey, T. et al. Inkjet printed circuits with 2D semiconductor inks for high-performance electronics. *Adv. Electron. Mater.* **7**, 2100112 (2021).
- Bossis, G. & Brady, J. F. The rheology of Brownian suspensions. *J. Chem. Phys.* **91**, 1866–1874 (1989).
- Yuan, Y. & Lee, T. R. *Contact Angle and Wetting Properties* (Springer, 2013).
- Liu, H. & Cao, G. Effectiveness of the Young-Laplace equation at nanoscale. *Sci. Rep.* **6**, 23936 (2016).
- Hyun, W. J. et al. Scalable, self-aligned printing of flexible graphene micro-supercapacitors. *Adv. Energy Mater.* **7**, 1700285 (2017).
- Kim, S. et al. Inkjet-printed antennas, sensors and circuits on paper substrate. *IET Microw. Antennas Propag.* **7**, 858–868 (2013).
- Carey, T. et al. Fully inkjet-printed two-dimensional material field-effect hetero-junctions for wearable and textile electronics. *Nat. Commun.* **8**, 1202 (2017).
- Woltornist, S. J. et al. Preparation of conductive graphene/graphite infused fabrics using an interface trapping method. *Carbon* **81**, 38–42 (2015).
- Huang, L., Huang, Y., Liang, J., Wan, X. & Chen, Y. Graphene-based conducting inks for direct inkjet printing of flexible conductive patterns and their applications in electric circuits and chemical sensors. *Nano Res.* **4**, 675–684 (2011).
- Kong, D., Le, L. T., Li, Y., Zunino, J. L. & Lee, W. Temperature-dependent electrical properties of graphene inkjet-printed on flexible materials. *Langmuir* **28**, 13467–13472 (2012).
- Gao, Y., Shi, W., Wang, W., Leng, Y. & Zhao, Y. Inkjet printing patterns of highly conductive pristine graphene on flexible substrates. *Ind. Eng. Chem. Res.* **53**, 16777–16784 (2014).
- Finn, D. J. et al. Inkjet deposition of liquid-exfoliated graphene and MoS<sub>2</sub> nanosheets for printed device applications. *J. Mater. Chem. C* **2**, 925–932 (2014).
- Seekaew, Y. et al. Low-cost and flexible printed graphene-PEDOT:PSS gas sensor for ammonia detection. *Org. Electron.* **15**, 2971–2981 (2014).
- Park, S.-H. et al. High areal capacity battery electrodes enabled by segregated nanotube networks. *Nat. Energy* **4**, 560–567 (2019).
- Tian, R. et al. Quantifying the effect of electronic conductivity on the rate performance of nanocomposite battery electrodes. *ACS Appl. Energy Mater.* **3**, 2966–2974 (2020).
- Tian, R. et al. Liquid exfoliated SnP<sub>3</sub> nanosheets for very high areal capacity lithium-ion batteries. *Adv. Energy Mater.* **11**, 2002364 (2021).
- Zhou, H., Zhu, S., Hibino, M., Honma, I. & Ichihara, M. Lithium storage in ordered mesoporous carbon (CMK-3) with high reversible specific energy capacity and good cycling performance. *Adv.* **15**, 2107–2111 (2003).
- Lian, P. et al. Large reversible capacity of high quality graphene sheets as an anode material for lithium-ion batteries. *Electrochim. Acta* **55**, 3909–3914 (2010).

65. Aurbach, D. Review of selected electrode-solution interactions which determine the performance of Li and Li ion batteries. *J. Power Sources* **89**, 206–218 (2000).
66. Xing, W. & Dahn, J. R. Study of irreversible capacities for Li insertion in hard and graphitic carbons. *J. Electrochem. Soc.* **144**, 1195–1201 (1997).
67. Levi, M. D. & Aurbach, D. The mechanism of lithium intercalation in graphite film electrodes in aprotic media. Part 1. High resolution slow scan rate cyclic voltammetric studies and modeling. *J. Electroanal. Chem.* **421**, 79–88 (1997).
68. Zhao, X. et al. Electrochemical exfoliation of graphene as an anode material for ultra-long cycle lithium ion batteries. *J. Phys. Chem. Solids* **139**, 109301 (2020).
69. Guo, Y.-G., Hu, J.-S. & Wan, L.-J. Nanostructured materials for electrochemical energy conversion and storage devices. *Adv* **20**, 2878–2887 (2008).
70. Taale, M. et al. Biomimetic carbon fiber systems engineering: a modular design strategy to generate biofunctional composites from graphene and carbon nanofibers. *ACS Appl. Mater. Interfaces* **11**, 5325–5335 (2019).
71. Liu, J., Cui, L. & Losic, D. Graphene and graphene oxide as new nanocarriers for drug delivery applications. *Acta Biomater.* **9**, 9243–9257 (2013).
72. Vranic, S. et al. Live imaging of label-free graphene oxide reveals critical factors causing oxidative-stress-mediated cellular responses. *ACS Nano* **12**, 1373–1389 (2018).
73. Hoyle, C. et al. Small, thin graphene oxide is anti-inflammatory activating nuclear factor erythroid 2-related factor 2 via metabolic reprogramming. *ACS Nano* **12**, 11949–11962 (2018).
74. Das, S. et al. Oxygenated functional group density on graphene oxide: its effect on cell toxicity. *Part. Part. Syst. Charact.* **30**, 148–157 (2013).

## ACKNOWLEDGEMENTS

XPS data were taken at NEXUS, Newcastle University, facility that was funded by UK Engineering and Physical Sciences Research Council (EPSRC), grant number NS/A000015/1. We have also received support from the Science Foundation Ireland (SFI) funded centre AMBER (SFI/12/RC/2278\_P2) and availed of the facilities of the SFI-funded AML and ARM labs. J.M.K acknowledges funding from Smart Quantum Dot Lighting (EPSRC, EP/P027628/1). T.C. acknowledges funding by a Marie Skłodowska-Curie Action “MOVE” (Grant Number 101030735).

## AUTHOR CONTRIBUTIONS

T.C. conceived the experiments. T.C. and J.C. directed the research and designed experiments. T.C. manufactured the inks and undertook Raman Spectroscopy with assistance from ADA. and J.M.K. T.C. undertook Inkjet printing, Rheology, Surface

tension and electrical measurements. H.K. and T.C. undertook AFM measurements. T. C. and J.M. undertook TGA measurements. A.A. and H.R.H. did all biological testing. T. C., A.K., D.H. and E.C. undertook SEM. R.T. and D.H. undertook the Li-ion battery testing. S.S. and L.S. undertook XRD and XPS measurements. The manuscript was written by T.C. in close consultation with other authors.

## COMPETING INTERESTS

The authors declare no competing interests.

## ADDITIONAL INFORMATION

**Supplementary information** The online version contains supplementary material available at <https://doi.org/10.1038/s41699-021-00279-0>.

**Correspondence** and requests for materials should be addressed to Tian Carey or Jonathan N. Coleman.

**Reprints and permission information** is available at <http://www.nature.com/reprints>

**Publisher's note** Springer Nature remains neutral with regard to jurisdictional claims in published maps and institutional affiliations.



**Open Access** This article is licensed under a Creative Commons Attribution 4.0 International License, which permits use, sharing, adaptation, distribution and reproduction in any medium or format, as long as you give appropriate credit to the original author(s) and the source, provide a link to the Creative Commons license, and indicate if changes were made. The images or other third party material in this article are included in the article's Creative Commons license, unless indicated otherwise in a credit line to the material. If material is not included in the article's Creative Commons license and your intended use is not permitted by statutory regulation or exceeds the permitted use, you will need to obtain permission directly from the copyright holder. To view a copy of this license, visit <http://creativecommons.org/licenses/by/4.0/>.

© The Author(s) 2022